JACS
JOURNAL OF THE AMERICAN CHEMICAL SOCIETY
Article
pubs.acs.org/JACS

Amorphous Mixed-Metal Oxide Thin Films from Aqueous Solution Precursors with Near-Atomic Smoothness

Matthew G. Kast, Elizabeth A. Cochran, Lisa J. Enman, Gavin Mitchson, Jeffrey Ditto, Chris Siefe, Paul N. Plassmeyer, Ann L. Greenaway, David C. Johnson, Catherine J. Page, and Shannon W. Boettcher*

Department of Chemistry and Biochemistry and the Materials Science Institute, University of Oregon, Eugene, Oregon 97403, United States

Supporting Information

ABSTRACT: Thin films with tunable and homogeneous composition are required for many applications. We report the synthesis and characterization of a new class of compositionally homogeneous thin films that are amorphous solid solutions of Al_2O_3 and transition metal oxides (TMO_x) including VO_x, CrO_x, MnO_x, Fe_2O_3, CoO_x, NiO, CuO_x, and ZnO. The synthesis is enabled by the rapid decomposition of molecular transition-metal nitrates $TM(NO_3)_x$ at low temperature along with precondensed oligomeric $Al(OH)_x(NO_3)_{3-x}$ cluster species, both of which can be processed from aq solution. The films are dense, ultrasmooth (R_{rms} < 1 nm, near 0.1 nm in many cases), and atomically mixed amorphous metal-oxide alloys over a large composition range. We assess the chemical principles that favor the formation of amorphous homogeneous films over rougher phase-segregated nanocrystalline films. The synthesis is easily extended to other compositions of transition and main-group metal oxides. To demonstrate versatility, we synthesized amorphous $V_{0.1}Cr_{0.1}Mn_{0.1}Fe_{0.1}Zn_{0.1}Al_{0.5}O_x$ and $V_{0.2}Cr_{0.2}Fe_{0.2}Al_{0.4}O_x$ with $R_{rms} \approx 0.1$ nm and uniform composition. The combination of ideal physical properties (dense, smooth, uniform) and broad composition tunability provides a platform for film synthesis that can be used to study fundamental phenomena when the effects of transition metal cation identity, solid-state concentration of d-electrons or d-states, and/or crystallinity need to be controlled. The new platform has broad potential use in controlling interfacial phenomena such as electron transfer in solar-cell contacts or surface reactivity in heterogeneous catalysis.

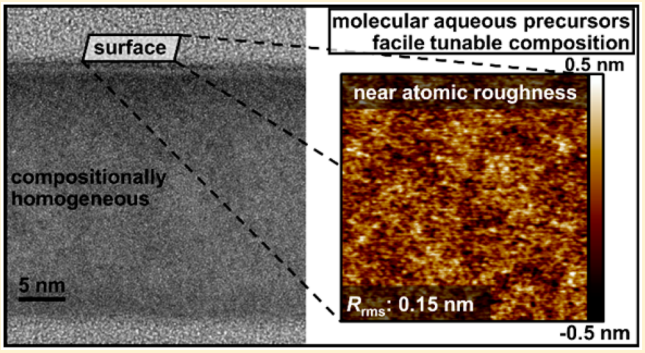

INTRODUCTION

Amorphous thin films are critical components of modern technology. Silica[1] and hafnium silicate[2,3] are used as gate dielectrics in advanced field-effect transistors (FETs); amorphous silicon (a-Si)/silicon nitride are used as contacts and passivation layers in high-efficiency crystalline silicon (c-Si) photovoltaics,[4−6] and amorphous indium-gallium-zinc oxide (a-IGZO) semiconducting channels are used as the active channel in thin-film transistors (TFTs).[7] Amorphous metals provide ultrasmooth electrodes in metal−insulator−metal tunnel diode devices.[8] Such practical utility is due to several factors. Amorphous films often make high-quality electronic interfaces due to the local bonding flexibility of the amorphous structure[9] without the material limitations and processing requirements of lattice-matched defect-free heteroepitaxy. They form ultrasmooth and uniform interfaces in contrast to polycrystalline thin films.[10] Amorphous silicates thus allow for passivation of c-Si surfaces with a minimal concentration of interface defect states,[11] as does hydrogenated a-Si[12] while also enabling selective charge extraction with appropriate contact engineering. Similarly, a-IGZO maintains high electron mobility in thin channels where the interface with the amorphous dielectric is a substantial fraction of the channel height. Amorphous materials are also kinetic products, which make their elemental composition unbounded by the compositional constraints of thermodynamic phase space. Silica, for example, can be alloyed with hafnium oxide to tune the dielectric response,[13] leakage current, and interface mobility. a-Si can be hydrogenated and heavily doped beyond the crystalline solid-solubility limit.[14] a-IGZO's carrier concentration and mobility can be tuned with the ratio of post-transition metals used.[15] Crystalline binary metal oxide alloys also allow for tuning bandgaps and band positions for solar-energy applications through controlling the cation electronic contribution to each band state.[16] Such principles should be directly applicable to amorphous mixed metal oxides.

Compared to bulk amorphous materials (e.g., oxide glasses), which are classically prepared by melt-quench processing,[17−20] thin films offer a broader range of nonequilibrium synthesis

Received: October 24, 2016
Published: December 3, 2016

DOI: 10.1021/jacs.6b11084
J. Am. Chem. Soc. 2016, 138, 16800−16808

techniques to access kinetically stable amorphous phases (e.g., sputtering, pulsed laser deposition, chemical vapor deposition, spin-casting, spray pyrolysis, etc.). These deposition methods collectively make use of rapid "chemical/physical quenching" processes whereby atomic or polyatomic species (molecules, ions, or radicals with high mobility) are quickly converted via chemical reaction into a 3D network with low solid-state ion mobility.[21] The range of compositions in which amorphous materials can be made in thin-film form by rapid chemical quench deposition methods has, however, not been investigated.

We demonstrate, using solution processing, the synthesis of ultrasmooth, dense, composition-controlled, mixed-metal oxide amorphous thin films of Al_2O_3 and the first-row transition-metal oxides (TMO_x; i.e., VO_x, CrO_x, MnO_x, Fe_2O_3, CoO_x, NiO, CuO_x, and ZnO). The approach uses a rapid chemical quench via a low-temperature heat treatment that drives precursor decomposition and oxide network formation. We note that other solution deposition routes have had success producing amorphous metal oxide films, in particular, aluminum oxide phosphate from an aerosol jet fog,[22] photochemical metal−organic deposition of transition metal oxides,[23] spin-casting of peroxide-stabilized precursors,[24,25] among other metal carboxylate- and alkoxide-based processes.[26] The films reported here have a root-mean-square surface roughness (R_{rms}) ≪ 1 nm and a tunable thickness and appear dense and defect-free by cross-sectional electron beam imaging. The driving forces that determine the maximum concentration of a given TMO_x that can be alloyed with Al_2O_3 and remain amorphous are discussed in light of the formation process's kinetics and energetics rooted in classical glass network theory. Across all TMO_x, amorphous solid solutions are observed when the mole fraction of TMO_x (to total metal content) is 10% or, presumably, less. Some TMO_x make amorphous solutions with Al_2O_3 to much higher concentrations of TMO_x (e.g., >50%) even though they readily crystallize when prepared alone. Those that phase-segregate yield thin-film materials consisting of crystalline transition metal oxide "c-TMO_x" nanoparticles that are embedded in an amorphous Al_2O_3 "a-Al_2O_3" matrix.

This work therefore lays the foundation for the simple preparation of amorphous oxides that can be designed for specific applications. For example, we note the need for new carrier-selective contacts to increase the efficiency of photovoltaics and photoelectrodes utilizing a wide variety of light-absorbing materials.[27,28] An ideal selective contact is optically tranparent,[28] makes an interface with the absorbing material that has a minimal concentration of recombination sites, and, critically, provides a large difference in resistance for electrons and holes so that it selects one over the other.[29] For example, thin-film alloys of Al_2O_3, a physically robust[30] network that passivates c-Si, and a TMO_x could provide access to materials where the electronic structure can be systematically tuned in the region of the valence and conduction bands to create multifunctional carrier-selective interfaces. Conduction band tunable electron-selective contacts have been made with amorphous In-Ga-O and Ga-Zn-Sn-O by Zhou et al. and show promise when used with organic photovoltaic absorber layers.[31] The ability to systematically and broadly tune composition has further applications in catalysis, for example, in tuning metal/oxide support interactions,[32,33] by providing atomically mixed heterogeneous active sites[23] or by allowing for systematic control over the oxide electronic structure and hence intermediate binding energies.[34] Amorphous metal oxide and multimetal perovskite oxides are also of interest in adaptive oxide devices.[35] The compositionally controlled, smooth, amorphous mixed-metal oxides developed here might enable tuning redox reactions and ion diffusion in adaptive oxide devices,[35] such as "memristors".[36] The amorphous alloy film platform presented here could also enable fundamental studies into amorphous dilute multimetal ferromagnetic oxide thin films.[37−39]

EXPERIMENTAL SECTION

Precursor Preparation. Solutions for spin-casting were prepared by mixing at different ratios 1 M aq solutions (prepared in 18.2 MΩ cm water) of transition-metal nitrate or chloride salts with 1 M aq $Al(NO_3)_x(OH)_{3-x}$ clusters, nominally "flat" $[Al_{13}(\mu_3-OH)_6(\mu-OH)_{18}(H_2O)_{24}](NO_3)_{15}$ or "f-Al_{13}" (to avoid confusion with the Keggin isomer).[40−42] Such clusters have been demonstrated to be excellent thin film precursors.[43] Fresh solutions were made <2 h prior to use for $Fe(NO_3)_3$- and $Mn(NO_3)_2$-containing precursors, which precipitate after extended exposure to air and light. Precursors containing V were prepared over ice by combining precooled solutions of 1 M VCl_3 and f-Al_{13}, which were allowed to react (as evident from bubble formation) for 5−10 min prior to spin coating. The final solutions were blue and thus presumably contained the vanadyl cation VO^{2+} with a combination of NO_3^- and Cl^- counterions. On the basis of the relative reduction potentials,[44] NO_3^- in f-Al_{13} oxidizes V^{3+} to V^{4+}, as evidenced by the color change from dark green (aq V^{3+}) to blue (aq VO^{2+}) upon reaction with f-Al_{13}. The reaction is more violent, and results in a brown precipitate if carried out at room temperature. The film compositions reported in the manuscript are those of the prepared precursor solution.

f-Al_{13} cluster solutions were made using a literature procedure. Briefly, 60 kC of reductive charge (at 150 mA) was passed per mole of $Al(NO_3)_3$ (1.5 M starting concentration) across an 80 cm^2 Pt mesh (working, reducing potential) and a small Pt coil (counter, oxidizing potential) electrodes in separate fritted compartments with stirring. This drives $Al(NO_3)_3$ oligomerization by consuming H^+ in the working electrode compartment and driving NO_3^- to the counter electrode compartment.[41] After electrolysis, the f-Al_{13} cluster solution concentration was standardized by thermogravimetric analysis of 2 mL of the solution after heating to 500 °C in a box furnace. At a final concentration of 1 M (relative to Al^{3+}), the f-Al_{13} solution had a pH of 3. TMO_x-P_2O_5 alloys were prepared by mixing transition metal nitrate solutions with 1 M phosphoric acid. Chemical supplier and purity info is provided in Table S1.

Thin Film Deposition. Single-side polished Si (100) substrates were scored with a diamond scribe on the unpolished side and cleaved into 2 × 2 cm squares. Substrates were loaded into a Teflon boat that held the samples in a vertical configuration. Substrates were washed in a sonicator for 10 min in a solution of 6.25% Contrad 70, rinsed with nanopure (18.2 MΩ) water for 30 s, loaded onto a spin-coater, spin rinsed for 10 s, spin dried for 20 s at 3000 rpm, and placed on a hot plate at 100 °C for 5 min to finish drying. The substrates were then plasma cleaned in an O_2/N_2 mixture for 10 min, spin rinsed with nanopure water for 5 s, and spin dried for 25 s. Precursor solution was deposited dropwise from a syringe through a 0.2 μm filter onto the substrate until the entire surface was wetted and then spun at 3000 rpm for 30 s. The sample was immediately moved to an Al block at 150 °C on a hot plate (as measured by a thermocouple embedded directly in the Al block). After 5 min at 150 °C, the samples were moved to a hot plate at 450 °C for 30 min.[15,40,45−48]

Characterization. X-ray reflectivity (XRR) data were collected on a Bruker D8-Discover using a Cu Kα X-ray source. Data were collected in a θ-2θ geometry after sample alignment.[49] Data were analyzed in Rigaku's GlobalFit software. Fourier transform fits were used to determine the R_{rms}.

X-ray diffraction (XRD) data were collected in a grazing incidence XRD (GIXRD) geometry on a Rigaku SmartLab. A Cu source was used. The incident angle of the X-ray beam was 0.5° relative to the sample plane, and the scintillation point detector was swept from 10 to

DOI: 10.1021/jacs.6b11084
J. Am. Chem. Soc. 2016, 138, 16800−16808

70° relative to the sample plane in 0.1° steps with an integration at each step of 30 s. A Ni filter was used to remove Cu Kβ interference.

Transmission electron microscopy (TEM) images were collected on an FEI Titan 80-300 utilizing a Gatan 2 K × 2 K CCD with an accelerating voltage of 300 keV. TEM samples (Al_2O_3 and $Fe_{0.5}Al_{0.5}O_x$) and all HAADF-STEM samples were cut out with a focused ion beam using an FEI Helios 600 FIB-SEM. One TEM sample ($Co_{0.4}Al_{0.6}O_x$) was removed physically by wetting with ethanol and scrapping the substrate prior to gently pulling a TEM grid (300 mesh lacey carbon/Cu) across the sample to transfer the sample from the substrate to the grid.

Atomic force microscopy (AFM) images were collected in tapping mode on a Bruker Dimension Icon. Si tapping mode probes (42 N m^{-1}, 320 kHz) were used. Images were collected over 500 nm square windows with 256 measurements per line and 256 lines per image at a scan rate of 1 Hz and scan velocity of 1 $\mu m\ s^{-1}$. Three images at different locations were collected. All images had first order flatten and third order plane fits applied. The instrument used has a 30 pm background noise level.

Elemental composition and spatial distribution was determined by scanning electron microscopy energy dispersive X-ray spectroscopy (SEM-EDS) using an FEI Helios 600 FIB-SEM. SEM images were collected with an accelerating voltage of 5 kV, and EDS images were collected with an accelerating voltage of 10 kV (Figures S4 and S5).

RESULTS AND DISCUSSION

We synthesized amorphous, near atomically smooth thin films of the electronic insulator Al_2O_3 alloyed with eight different transition metal oxides and combinations of these. First, we discuss the design of the aqueous precursor chemistry that enables the solution synthesis of these new materials. We then provide a detailed analysis of the formation processes and solid-state chemistry and discuss how dense amorphous thin films can be designed and synthetically targeted.

Synthesis of Mixed-Metal Amorphous Oxide Films from Solution. Deposition via spin coating of a dissolved species generally proceeds through two phases.[50] During the first phase, mass is lost from the film as material is flung from the substrate until a steady-state thickness of precursor solution is established, which depends on the rotational speed, substrate diameter, solution surface tension, solution viscosity, and substrate surface energy. In the second phase, the solution concentrates as solvent evaporates from the top surface of the liquid phase film,[50,51] driving precipitation of the solid film precursor as either polycrystalline or amorphous materials (which often incorporate solvent as gels).

With these processes in mind, there are several design parameters for precursors needed to make dense, amorphous, smooth, mixed-metal oxide films. When multiple metal salts are used, they must be cosoluble (at least kinetically on the time frame of spin processing). The solvent vapor pressure of the saturated (and likely the supersaturated) precursor film (here water) must be sufficiently high. Precursors with low solvent vapor pressures form poor films as they do not dry and gel during the spinning stage. For example, films deposited from 1 M aq $AlCl_3$ resulted in very poor film quality. The deposited precursor remained liquid after the spinning step due to the hygroscopic nature of $AlCl_3$ and thus did not form a mechanically stable thin-film gel during spinning. The precursors should also have a minimal number of coordinating ligands or counterions, as removal of these upon heating can lead to porosity.[15] The counterions should also decompose at low temperature, as do many nitrate salts, to allow for chemical quenching of mixed-metal oxide films.

We have designed our synthetic approach with these criteria in mind. We utilize oligomeric f-Al_{13}[40−42] as one component of the precursor solution and combine it with nitrate salts of Cr, Mn, Fe, Ni, Co, Cu, or VCl_3. The f-Al_{13} clusters are synthesized by simple electrolysis of $Al(NO_3)_3$ salt solutions across a glass frit. The electrolysis consumes protons and increases the Al^{3+}:NO_3^- ratio in the precursor solution, driving oligomerization and cluster formation. Cluster/oligomer precursors provide smooth dense amorphous aluminum oxide thin films with physical and electronic properties approaching those of ALD-deposited alumina.[40,43] The clusters are soluble at pH ∼3 and compatible with a large number of transition-metal nitrate precursors that are also stable under mildly acidic conditions. Because the f-Al_{13} clusters are partially condensed, they have relatively few counterions that must be decomposed upon heating, leading to high film density. The large f-Al_{13} oligomers mix with the transition-metal nitrate salts homogeneously and appear to prevent salt crystallization at room temperature due their large size and low diffusivity. All of the mixed oxides thus remain smooth and amorphous with sufficient Al content, whereas the single-component metal oxide films do not.

After spin-casting, the films are dried on a hot plate at 150 °C and rapid color changes due to reflective interference are observed as the solvent evaporates and the film thickness decreases. Nitrate anions also leave in the form of water/nitric acid azeotropes (boiling point of 120 °C).[38] During a second annealing step at 450 °C for 30 min, the nitrates fully decompose, presumably leaving as various NO_x gases, and the precursor film is converted into a dense oxide by condensation of hydroxides to form bridging oxide bonds.[15,40,46,47,52,53] We refer to this annealing step as a chemical quenching because the bridging metal oxide chemical bonds formed at low temperature may kinetically stabilize the initial amorphous film.

Thin Film Characterization: Film Quality and Amorphous Nature. Figure 1 shows GIXRD data collected on 30 nm thick films of $TM_yAl_{1-y}O_x$ and $TM_yP_{1-y}O_x$, where TM is a transition metal cation. $Co^{3+/2+}$, Ni^{2+}, and Cu^{2+} phase segregate at $y \geq 0.3$; diffraction peaks can be indexed to known oxide phases (spinel Co_3O_4,[54] rock salt NiO,[55] and tenorite CuO,[56] respectively). Films containing $V^{4+/5+}$, $Cr^{3+/6+}$, Mn^{3+}, Fe^{3+}, and Zn^{2+} do not show clear Bragg diffraction until higher concentrations of TM, indicating different crystallization and phase segregation kinetics and energetics, as discussed below. When they do crystallize, they crystallize as Shcherbinaite-V_2O_5,[57] α-Cr_2O_3,[58] α-Mn_2O_3,[59] α-Fe_2O_3,[60] and hexagonal ZnO,[61] respectively. No periodic trend in crystallization behavior is evident from these data.

To assess the possibility of small crystallites in the films that appear amorphous by X-ray techniques, we used transmission electron microscopy (TEM) and energy dispersive X-ray spectroscopy (EDS). Figure 2 shows high-resolution TEM cross sections prepared by focused ion beam milling of Al_2O_3 and $Fe_{0.5}Al_{0.5}O_x$. In addition, a powder TEM image of $Co_{0.4}Al_{0.6}O_x$, which was mechanically removed from the substrate, is shown. The Al_2O_3 and $Fe_{0.5}Al_{0.5}O_x$ films appear amorphous and nearly featureless and show Å-level roughness at both interfaces. Crystallites with d-spacing that match the Co_3O_4 phase are apparent in the TEM image of $Co_{0.4}Al_{0.6}O_x$. Additionally, a TEM-EDS line scan across the depth of the $Fe_{0.5}Al_{0.5}O_x$ film (Figure S2) shows uniform distribution of both Fe and Al. HAADF-STEM was also used to probe the presence of crystallites in the films. These data are shown in Figure S3 and also indicate a lack of crystalline phase-

DOI: 10.1021/jacs.6b11084
J. Am. Chem. Soc. 2016, 138, 16800−16808

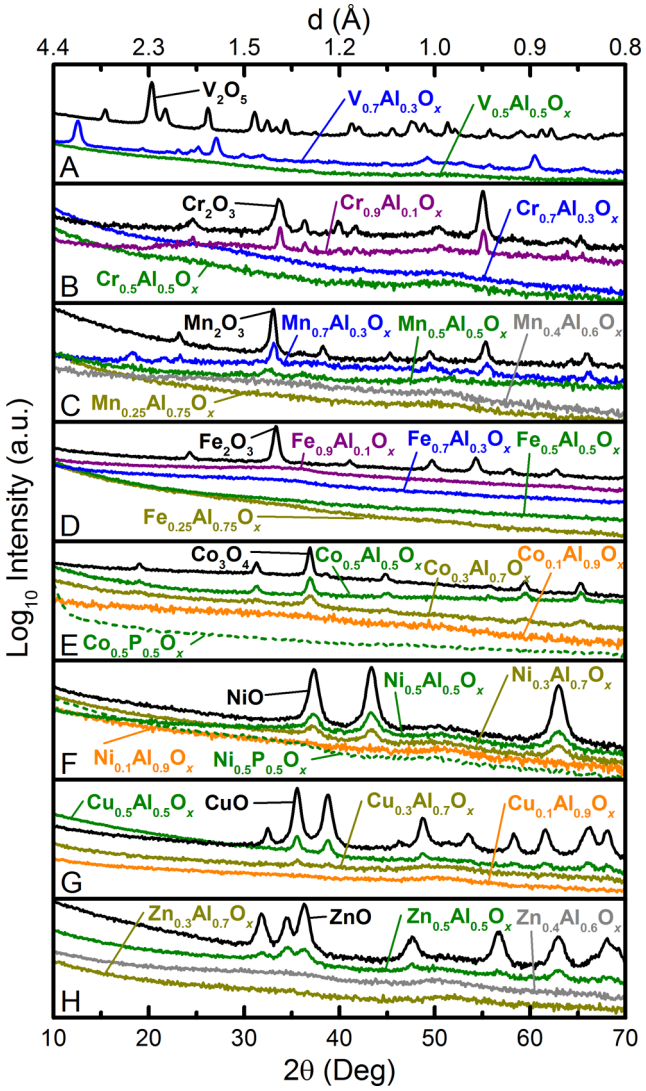

Figure 1. GIXRD patterns of (A) $V_yAl_{1-y}O_x$, (B) $Cr_yAl_{1-y}O_x$, (C) $Mn_yAl_{1-y}O_x$, (D) $Fe_yAl_{1-y}O_x$, (E) $Co_yAl_{1-y}O_x$, (F) $Ni_yAl_{1-y}O_x$, (G) $Cu_yAl_{1-y}O_x$, and (H) $Zn_yAl_{1-y}O_x$ with y = 1 (black), 0.9 (purple), 0.7 (blue), 0.5 (green), 0.4 (dark gray), 0.25 or 0.3 (dark yellow), and 0.1 (orange). Panels (E) and (F) also show GIXRD patterns of $Co_{0.5}P_{0.5}O_x$ and $Ni_{0.5}P_{0.5}O_x$ films, respectively, with dashed green lines. All films were annealed at 450 °C for 30 min. $Mn_{0.7}Al_{0.3}O_x$ and $V_{0.7}Al_{0.3}O_x$ stand out as films that show minimal and significant differences, respectively, in their crystallization behavior compared to the pure TMO_x films. $Mn_{0.7}Al_{0.3}O_x$ shows one extra diffraction peak at 18.2° and shoulders on some of the larger peaks; these are likely due to the presence of different MnO_x phases with slightly different Mn oxidation states and stoichiometries. The phase(s) present in the $V_{0.7}Al_{0.3}O_x$ film are illustrated in Figure S1.

segregated components. SEM and SEM-EDS were carried out on a select number of films to further probe the morphology and demonstrate homogeneity of elemental distribution in the films (Figure S4). EDS was also used to probe the (approximate) ratio of transition metal to total metal in the films, and the composition trended with the precursor solution composition as expected (Figure S5). Previous work on solution-processed films has further demonstrated that the solution composition defines the final film composition, as expected by the spin-casting mechanism discussed above for precursors that form nonvolatile oxides.[15,51]

For understanding the effect of phase segregation on film morphology, roughness was measured with XRR (Figure 3) and AFM (Figure 4). XRR data are used to assess the average correlation of the two interfaces of a film, and this can be interpreted as a roughness, although such interpretation requires a homogeneous electron density throughout the film.[49] AFM provides a microscopic measure of the surface roughness (convoluted with the tip radius) and an image of the local morphology.[62] For these reasons, roughness measured by XRR is not usually equivalent to that measured by AFM, although the trends are similar (Figure 5). Films that lack Bragg diffraction intensity (i.e., that are hypothesized to be amorphous alloys) show no substantial increase in roughness compared to that of a pure Al_2O_3 film (i.e., $R_{rms} \approx 0.1$ nm). Films composed of transition-metal crystallites and alumina show increased R_{rms} of 1−2 nm, i.e., approximately an order of magnitude larger than the amorphous films. As is evident from AFM images of $Ni_{0.5}Al_{0.5}O_x$, the increased roughness is correlated with crystalline grain growth and phase segregation (Figure 4). We have used XRR data to additionally estimate the density of the films (Figure S6). The films have estimated densities of between 60 and 80% of the relevant crystalline film components, consistent with their amorphous structure.

The low R_{rms} of the amorphous compositions (1−2 Å for Fe, Co, Ni, Cu, and Zn and 3−10 Å for V, Cr, and Mn) compare favorably with state-of-the-art deposition techniques such as ALD, under ideal conditions.[63] This exceptional smoothness corresponds to the distance of two metal−oxygen bonds and makes integration into devices for a variety of applications feasible even for films only a few nm in thickness.[64] Accessing such amorphous mixed-metal oxide films with controlled composition in an ultrasmooth morphology would be difficult by other techniques. Both chemical vapor and atomic layer deposition techniques are highly sensitive to the individual precursor and cross reactivity when ternary, quaternary, and higher order compositions are targeted. Significant precursor design work is needed to enable any given composition.[65,66] Physical vapor deposition techniques (sputter, pulsed-laser deposition, evaporation) are dependent on a custom target for each film composition or a deposition system with multiple targets or crucibles and controlled power to each.[67]

Although primarily binary metal oxides were investigated here, the approach enables complex films with mixtures of many different cations. Proof-of-principle four- and six-component films are illustrated in the final section below, after we first discuss the chemical principles enabling amorphous film synthesis.

Film Formation and the Driving Forces for Phase Segregation. Electronic applications of mixed-metal oxide films require smooth surfaces and homogeneous composition. The data above demonstrate that the solution deposition and "chemical quenching" approach enables the synthesis of amorphous films with near atomic smoothness over a large compositional space. Some compositions, however, yield amorphous films over larger composition ranges than others. Understanding the fundamental physical and chemical interactions that lead to amorphous or phase-segregated films (summarized in Figure 6A) is therefore important to guide further synthetic efforts and enable applications.

Film formation proceeds through evaporation of solvent at room temperature, the removal of nitrates and water by evaporation of the nitric acid/water azeotrope at intermediate temperatures, and the decomposition of $TM(NO_3)_x$ to TMO_x

DOI: 10.1021/jacs.6b11084
J. Am. Chem. Soc. 2016, 138, 16800−16808

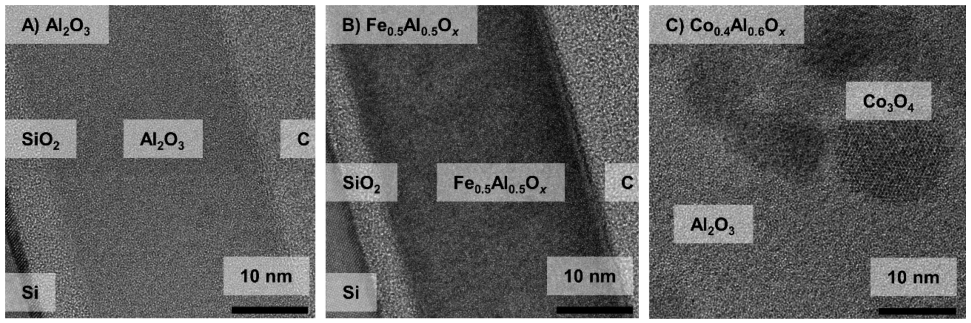

Figure 2. TEM images of (A) Al_2O_3, (B) $Fe_{0.5}Al_{0.5}O_x$, and (C) $Co_{0.4}Al_{0.6}O_x$. Note that there are no apparent crystalline regions in the Al_2O_3 and $Fe_{0.5}Al_{0.5}O_x$ films, whereas phase segregation is apparent in $Co_{0.4}Al_{0.6}O_x$.

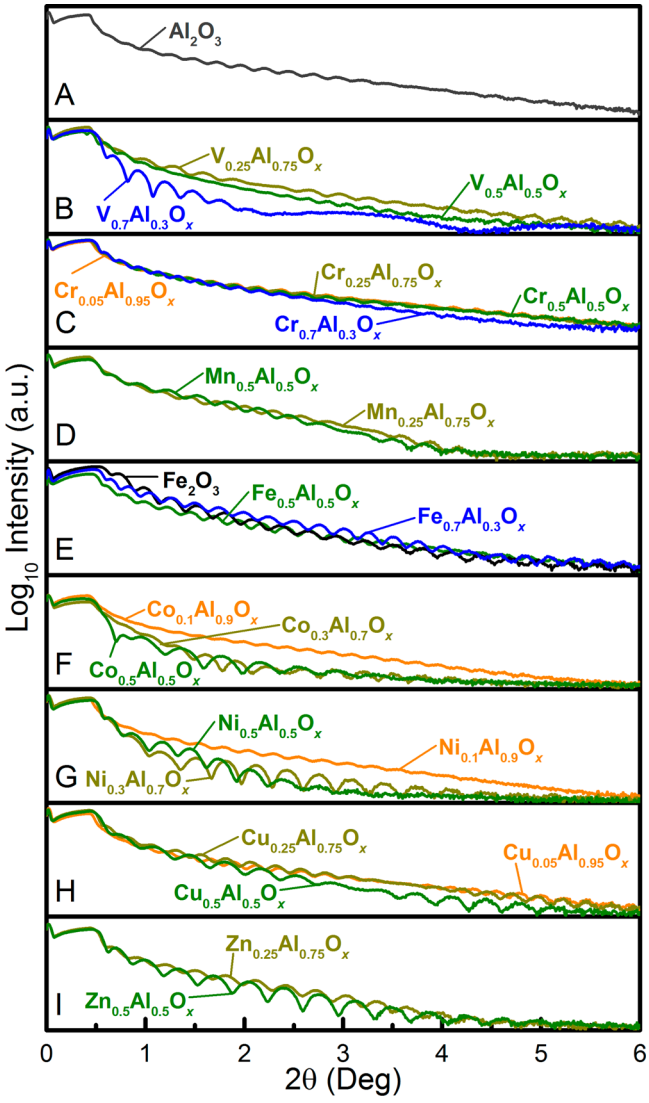

Figure 3. XRR of (A) Al_2O_3, (B) $V_yAl_{1-y}O_x$, (C) $Cr_yAl_{1-y}O_x$, (D) $Mn_yAl_{1-y}O_x$, (E) $Fe_yAl_{1-y}O_x$, (F) $Co_yAl_{1-y}O_x$, (G) $Ni_yAl_{1-y}O_x$, (H) $Cu_yAl_{1-y}O_x$, and (I) $Zn_yAl_{1-y}O_x$ with y = 1 (black), 0.9 (purple), 0.7 (blue), 0.5 (green), 0.25 or 0.3 (dark yellow), and 0.1 or 0.05 (orange). For each TMO_x, the roughness is higher when TMO_x crystallites are present. In some cases, the films become sufficiently rough that interference effects needed for resolving the Kiessig fringes are lost.

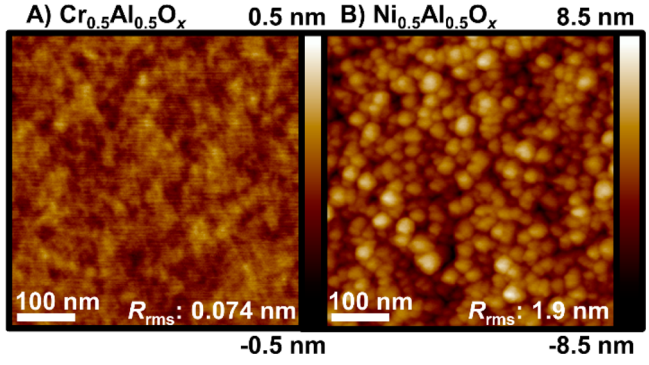

Figure 4. Representative AFM images of (A) an amorphous film ($Cr_{0.5}Al_{0.5}O_x$) and (B) a film with transition-metal crystallites ($Ni_{0.5}Al_{0.5}O_x$). Note the near-atomic roughness of the amorphous films and the defined particulate structure present in the $Ni_{0.5}Al_{0.5}O_x$ sample, presumably consisting of NiO crystallites protruding above the surface of the amorphous Al_2O_3.

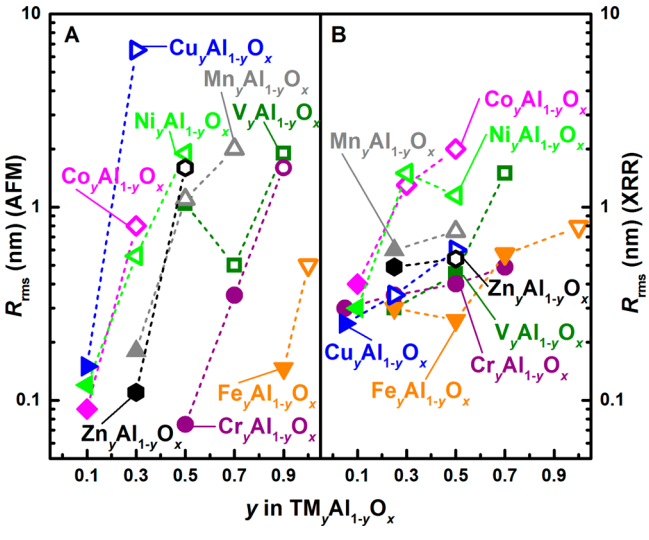

Figure 5. (A) R_{rms} measured by AFM and (b) XRR as a function of the alloy identity (label) and the concentration of the TMO_x in the films. Amorphous solid solutions are shown with solid markers, and segregated mixtures of transition metal oxide crystallites and amorphous alumina are shown with open markers. Note the dramatic increase in roughness in most films that contain segregated crystallites (indicated by open markers).

at elevated temperatures. The formation of $TM_yAl_{1-y}O_x$ is dependent on the precipitation of f-Al_{13} and $TM(NO_3)_x$ to form a gelled, atomically mixed precursor film and the decomposition of the $TM_yAl_{1-y}(OH)_x(NO_3)_z$ gel to yield $TM_yAl_{1-y}O_x$. Differences in either the solubility of the

DOI: 10.1021/jacs.6b11084
J. Am. Chem. Soc. 2016, 138, 16800−16808

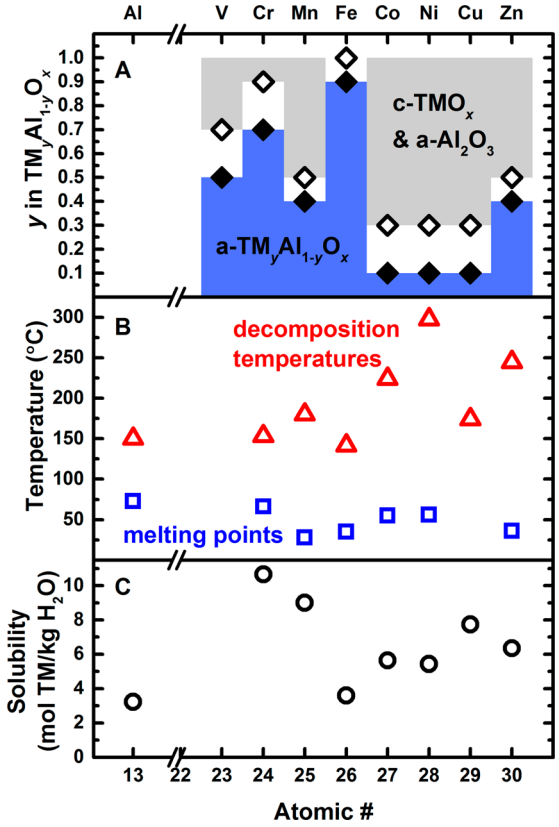

Figure 6. (A) Regions of TMO_x identity and concentration where a-$TM_yAl_{1-y}O_x$ and c-TMO_x/a-Al_2O_3 are formed, (B) decomposition temperatures (red triangles) and melting points (blue squares), and (C) solubilities of the individual (i.e., pure) $TM(NO_3)_x$ salts as well as for pure $Al(NO_3)_3$. In (A), solid diamonds represent a sample measured to be amorphous (in Figure 1); open diamonds represent a sample with crystalline transition metal oxide particulates (also from Figure 1), and the white space between these two boundaries is the region of composition space that has not been measured. The transition between amorphous solid solutions and particulate mixtures occurs in this region. The decomposition and melting temperatures of f-Al_{13} were determined to be similar to $Al(NO_3)_3$. Decomposition temperature and solubility are not listed for V as it likely forms a $VO(NO_3)_x(Cl)_y$ species in the precursor solution. Accurate solubility and decomposition data do not exist for this species, although there are reports that it decomposes to V_2O_5 upon drying.[69] The decomposition temperature was defined here as the temperature at which the precursor had lost 75% of the total mass lost at high temperature where oxide phases are formed.

$TM(NO_3)_x$ relative to that of f-Al_{13} or a large difference in the decomposition temperature of $TM(NO_3)_x$ relative to that of f-Al_{13} might thus cause phase segregation.

The aqueous solubilities of the metal nitrates studied span a range of 1−10 M (Figure 6C). CoO_x, NiO, and CuO_x phase segregate readily in the mixed oxide thin films, but their nitrate salts have moderate solubilities that are higher than $Fe(NO_3)_3$ and lower than $Cr(NO_3)_3$, which both remain amorphous to high concentrations of transition metal. This analysis suggests precursor solubility is not the dominant effect driving phase segregation. It is likely that under the rapid evaporation conditions prevalent during spin coating that precipitation occurs sufficiently fast that the different precursors coprecipitate even though they may have different solubilities. Further, the hydrated metal nitrates used have melting points between 25 and 75 °C, as shown in Figure 6B, which are below their decomposition temperature. The metal nitrates may thus melt prior to decomposition during the annealing process, allowing for further mixing.

Bulk thermogravimetric analysis of each $TM(NO_3)_x$ was carried out (Figure S3) to determine the precursor decomposition temperature and is plotted in Figure 6B along with melting points of the pure $TM(NO_3)_x$ obtained from the literature.[68] Corresponding melting point and decomposition values for $Al(NO_3)_3$ are plotted in Figure 6B. $Ni(NO_3)_2$, $Co(NO_3)_2$, and $Zn(NO_3)_2$ have higher decomposition temperatures than the other $TM(NO_3)_x$. Co_3O_4 and NiO readily phase segregate at more than ∼10% concentration, suggesting differences in decomposition temperature between the $TM(NO_3)_2$ and f-Al_{13} drive phase segregation. The fact that ZnO does not segregate until higher compositions is likely related to its d^{10} electron count and concurrent higher local flexibility relative to $Co^{2+}(d^7)$, $Ni^{2+}(d^8)$, and $Cu^{2+}(d^9)$, as discussed below.

Because $V(NO_3)_x$ salts are not stable, VCl_3 and f-Al_{13} were used for the $V_yAl_{1-y}O_x$ precursor. When this precursor is mixed on ice, NO_3^- slowly oxidizes V^{3+} to V^{4+}. Because of this, accurate solubilities and decomposition temperatures for the relevant V-containing precursor are not available.

Local Chemical Bonding Effects. The degree to which a particular oxide retains an amorphous structure might be rationalized by the coordinative flexibility of the oxygen anions around the transition metal cations. Table 1 summarizes the composition range over which amorphous mixed metal or phase-segregated nanocrystalline $TM_yAl_{1-y}O_x$ thin films were found and the proposed reason(s) for the formation of amorphous films that are discussed in this section.

Table 1. Overview of Amorphous Film Composition and Formation

TMO_x	range amorphous for $TM_yAl_{1-y}O_x$	range phase segregated c-TMO_x a-Al_2O_3	rationale for amorphous range[a]
VO_x	$y \le 0.5$	$y \ge 0.7$	high Q_M, low C_O, d^0
CrO_x	$y \le 0.7$	$y \ge 0.9$	high Q_M, low C_O, d^0
MnO_x	$y \le 0.4$	$y \ge 0.5$	mod. Q_M, mod. C_O
FeO_x	$y \le 0.9$	$y = 1$	mod. Q_M, low C_O, d^5-HS
CoO_x	$y \le 0.1$	$y \ge 0.3$	dilute only
NiO	$y \le 0.1$	$y \ge 0.3$	dilute only
CuO_x	$y \le 0.1$	$y \ge 0.3$	dilute only
ZnO	$y \le 0.4$	$y \ge 0.5$	mod. C_O, d^{10}

[a] Q_M = oxidation state of the metal cations, C_O = coordination number of oxygen anions, $d^0/d^5/d^{10}$ = electron occupancy of the d-states in the transition metal cation.

On the basis of early glass network theory by Zachariasen, the coordination of the oxygen anions in the metal oxide network affects the energetic stability of amorphous oxide systems.[18−20,70,71] The coordination of oxygen (C_O) can be calculated if the coordination of cations (C_M, based on the coordination geometry), oxidation state of the cations (Q_M), and oxidation state of oxygen (Q_O) are known[72]

$$C_O = \frac{C_M|Q_O|}{|Q_M|} \quad (1)$$

Lower coordination on oxygen anions results in more-open metal oxide networks (illustrated in Figure S4). The energetic stability of open networks is less dependent on the crystallinity

DOI: 10.1021/jacs.6b11084
J. Am. Chem. Soc. 2016, 138, 16800−16808

of the system than would be the case for a closed network due to the fact that short-range order can be maintained on the metal centers in a sufficiently open network even when no long-range order is present. If there exists insufficient openness in the network, strain/distortion must be applied to the local coordination to maintain an amorphous structure; this is energetically unfavorable compared to forming a closed crystalline network. Distortion applied to the local coordination environment is especially unfavorable when the coordinated cations have partially filled d-states due to their ligand field stabilization energy (LFSE).

The occupancy of the d-states and the LFSE can be used as a measure of the degree of preference for a particular local structure over another.[73] If the d-states are fully occupied (d^{10}), unoccupied (d^0), or exactly half occupied with no paired electrons "high spin" (d^5-HS), there is no preference for one coordination environment over another due to electronic effects. V^{5+} and Cr^{6+} are d^0; Fe^{3+} is d^5-HS, and Zn^{2+} is d^{10}. The energetic penalty for these cations to be in multiple coordination environments is less than that of Mn^{3+}, $Co^{2+/3+}$, Ni^{2+}, or Cu^{2+}. The d^0, d^{10}, and d^5-HS cations can thus adopt low-coordination tetrahedral environments resulting in more open networks (eq 1). In particular, this is likely why ZnO forms amorphous alloys in $TM_yAl_{1-y}O_x$ until $y = 0.4$, whereas CoO_x, NiO, and CuO_x phase segregate unless $y \leq 0.1$.

$TM_yAl_{1-y}O_x$ films containing V or Cr cations stay amorphous to high concentrations of TM, $y = 0.5$ and 0.7, respectively. Both V and Cr cations likely have average formal charges $>3^+$, which are larger than the other cations in this study. As seen from the diffraction data (Figure 1), VO_x crystallizes with V in the 5+ oxidation state. XPS data of Cr-containing films show the presence of Cr^{6+} (Figure S5). High oxidation states lead to lower coordination numbers of the oxygen anions if the coordination geometry is unchanged (eq 1), which stabilizes the amorphous state as discussed above. Higher cation oxidation states also result in higher activation energies for cation hopping and thus slower cation diffusion (as discussed further below).[74−76] MnO_x's intermediate oxidation state, +3 when it crystallizes, may allow for amorphous alloys with Al_2O_3 when $y \leq 0.4$ but not at the higher concentrations possible for the Al_2O_3 and VO_x or CrO_x systems.

CoO_x, NiO, and CuO_x only alloy with Al_2O_3 in the amorphous state when $y \leq 0.1$. This is likely due to their nonzero LFSE and low oxidation state. The fact that they remain amorphous at $y = 0.1$ is likely because the TM cations are dilute in the amorphous matrix, which allows for kinetic trapping during synthesis. Entropy may also stabilize $Co_yAl_{1-y}O_x$, $Ni_yAl_{1-y}O_x$, and $Cu_yAl_{1-y}O_x$ thin films in the mixed amorphous state at $y = 0.1$, as has been observed in mixed crystalline oxide systems.[77]

If the stability of the mixed-metal alloy is indeed dependent on the coordination around network O, then replacing Al^{3+} with a glass-forming cation of higher oxidation state and/or lower coordination number will result in a larger range of compositions that yield amorphous alloys. P_2O_5 is an ideal glass former with a high cation field strength, high oxidation state (5+), and tetrahedral coordination that forms robust open networks.[71] Although also very hygroscopic and thus unlikely practical for electronic applications, P_2O_5 is a useful host to test the fundamental network forming chemistry in comparison to Al_2O_3. Figure 1 (dashed lines) demonstrates that amorphous alloys can be synthesized with 50% Co or Ni in P_2O_5, whereas films of similar composition in the Al_2O_3 phase segregate, consistent with the hypothesis presented above.

Kinetic Barriers to Phase Segregation: Metal Diffusion Coefficients. Our data (Figure 1) show that cations with higher oxidation states (6+, 5+, 3+) are more stable in amorphous alumina films than those of lower oxidation states (2+). Typical trivalent cations have activation energies of diffusion of over ~4 eV in metal oxides,[74] typical divalent metals in the range of 2 eV in metal oxides,[75,76] and typical monovalent metals of 0.15 eV and higher.[78] Because the activation barrier for self-diffusion of a transition metal oxide should be related to the metal oxygen bond strength, the trend in activation energy may help explain the experimental observation that high-oxidation-state cations are more likely to form amorphous phases. Furthermore, this implies that the activation energy for diffusion of higher oxidation state metals will be larger than those with lower oxidation states in the films through all stages of the formation process. Thus, the kinetics of molecular rearrangement are likely to contribute significantly to the materials' tendency to form amorphous or polycrystalline films.

Complex Film Stoichiometries. To demonstrate the compositional flexibility of the solution chemistry platform while maintaining a single-phase dense amorphous film with "atomic" smoothness, we fabricated four- and six-component metal oxide thin films (Figure 7). By selecting transition metal oxides with high oxidation states, keeping the individual TMO_x fraction low (10%) and the Al_2O_3 fraction moderate (50%), amorphous $V_{0.1}Cr_{0.1}Mn_{0.1}Fe_{0.1}Zn_{0.1}Al_{0.5}O_x$ was deposited with a 0.1 nm R_{rms}. Using TMO_x with only high oxidation states and d^0 or d^5-HS electronic configurations enabled the synthesis of

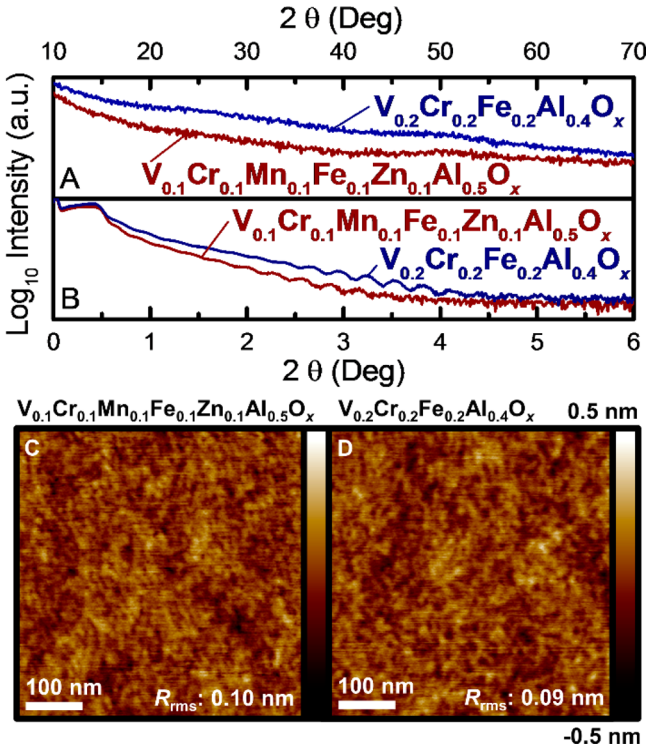

Figure 7. (A) GIXRD, (B) XRR, and (C and D) AFM of $V_{0.1}Cr_{0.1}Mn_{0.1}Fe_{0.1}Zn_{0.1}Al_{0.5}O_x$ and $V_{0.2}Cr_{0.2}Fe_{0.2}Al_{0.4}O_x$ films deposited by spin coating and annealed at 450 °C. Note the lack of Bragg diffraction from any phase and that R_{rms} is ≤ 0.1 nm.

DOI: 10.1021/jacs.6b11084
J. Am. Chem. Soc. 2016, 138, 16800−16808

the quaternary alloy $V_{0.2}Cr_{0.2}Fe_{0.2}Al_{0.4}O_x$ with a single amorphous phase and subangstrom roughness (R_{rms} = 0.09 nm). These were the only two complex compositions attempted. It should therefore be straightforward to synthesize a large number of other compositions for specific applications following the guiding principles outlined in the above section.

CONCLUSIONS

We report the synthesis and characterization of a new family of precise, near atomically smooth, thin-film amorphous oxide alloys. These materials are inaccessible by traditional bulk melt-quench methods and made possible here by design of aqueous precursor chemistry and chemical quenching of the amorphous state in the spin-cast solution precursor film. The synthesis allows for easy composition tuning, including access to complex amorphous compositions with four and six metal oxide components, while delivering dense uniform amorphous films. We discovered significant differences in the highest amount of 3d transition metals that can be alloyed with alumina in the amorphous state. We explain the trends in amorphous-alloy stability using concepts from glass theory and inorganic and solid-state chemistry: (1) low oxygen coordination yields open networks that stabilize amorphous structure by minimizing local strains, (2) d^0, d^5-HS, and d^{10} metals yield high bonding/coordination flexibility, and (3) high metal oxidation states increase activation energy for cation hopping, suggesting kinetic stabilization of the chemically quenched amorphous state. The dramatic tunability of the amorphous film composition suggests a route to systematically affect film electronic structure while maintaining exceptional film smoothness. This broad and flexible synthetic platform allows targeted design of new materials systems for a range of applications including "selective" electronic contacts and multicomponent heterogeneous catalysts.

ASSOCIATED CONTENT

Supporting Information

The Supporting Information is available free of charge on the ACS Publications website at DOI: 10.1021/jacs.6b11084.

Chemical details, GIXRD, TEM-EDS line scans, HAADF-STEM, SEM, SEM-EDS, XRR, TGA, XPS, and AFM data, and schematic of open and closed networks (PDF)

AUTHOR INFORMATION

Corresponding Author

*swb@uoregon.edu

ORCID

Catherine J. Page: 0000-0002-4545-7835

Shannon W. Boettcher: 0000-0001-8971-9123

Notes

The authors declare no competing financial interest.

ACKNOWLEDGMENTS

Brittany Gordon and Julija Vinckeviciute are thanked for exploratory work on mixed-metal oxide systems. Michaela Burke Stevens is thanked for insightful discussions. Josh Raznik is thanked for collecting TEM data. Robert Fischer is thanked for collecting a portion of the SEM and EDS data. This work was funded by National Science Foundation (NSF) grant CHE-1102637 through the Center for Sustainable Materials Chemistry. The CAMCOR shared instrument facilities (XRD, XRR, AFM, TEM, XPS, and SEM in this study) are supported by grants from the W.M. Keck Foundation, the M.J. Murdock Charitable Trust, ONAMI, the Air Force Research Laboratory (FA8650-05-1-5041), NSF (0923577 and 0421086), and the University of Oregon. We also acknowledge support through the Collaborative Access Team (CAT): Pooled Resources for Electron Microscopy Informatics, Education and Research (PREMIER) Network Program at Pacific Northwest National Laboratory (PNNL) and the Environmental Molecular Sciences Laboratory, a national scientific user facility sponsored by DOE's Office of Biological and Environmental Research at PNNL. PNNL is a multiprogram national laboratory operated by Battelle for DOE under Contract DE-AC05-76RL01830. S.W.B. acknowledges support from the Research Corporation for Science Advancement as a Cottrell Scholar.

REFERENCES

(1) Tanenbaum, M.; Valdes, L. B.; Buehler, E.; Hannay, N. B. *J. Appl. Phys.* **1955**, *26* (6), 686−692.

(2) Wilk, G. D.; Wallace, R. M. *Appl. Phys. Lett.* **1999**, *74* (19), 2854−2856.

(3) Kingon, A. I.; Maria, J.; Streiffer, S. K. *Nature* **2000**, *406*, 1032−1038.

(4) Cousins, P. J.; Smith, D. D.; Luan, H.-C.; Manning, J.; Dennis, T. D.; Waldhauer, A.; Wilson, K. E.; Harley, G.; Mulligan, W. P. In *35th IEEE Photovoltaic Specialists Conference*; 2010; pp 275−278.

(5) Masuko, K.; Shigematsu, M.; Hashiguchi, T.; Fujishima, D.; Kai, M.; Yoshimura, N.; Yamaguchi, T.; Ichihashi, Y.; Mishima, T.; Matsubara, N.; Yamanishi, T.; Takahama, T.; Taguchi, M.; Maruyama, E.; Okamoto, S. *IEEE J. Photovoltaics* **2014**, *4* (6), 1433−1435.

(6) Green, M. A.; Emery, K.; Hishikawa, Y.; Warta, W.; Dunlop, E. D. *Prog. Photovoltaics* **2015**, *23*, 1−9.

(7) Nomura, K.; Ohta, H.; Takagi, A.; Kamiya, T.; Hirano, M.; Hosono, H. *Nature* **2004**, *432*, 488−492.

(8) Cowell, E. W., III; Alimardani, N.; Knutson, C. C.; Conley, J. F.; Keszler, D. A.; Gibbons, B. J.; Wager, J. F. *Adv. Mater.* **2011**, *23*, 74−78.

(9) Lucovsky, G.; Wu, Y.; Niimi, H.; Misra, V.; Phillips, J. C. *Appl. Phys. Lett.* **1999**, *74* (1999), 1−3.

(10) Jiang, K.; Meyers, S. T.; Anderson, M. D.; Johnson, D. C.; Keszler, D. A. *Chem. Mater.* **2013**, *25*, 210−214.

(11) Eades, W. D.; Swanson, R. M. *J. Appl. Phys.* **1985**, *58* (11), 4267−4276.

(12) Aberle, A. G. *Prog. Photovoltaics* **2000**, *8*, 473−487.

(13) Callegari, A.; Cartier, E.; Gribelyuk, M.; Okorn-Schmidt, H. F.; Zabel, T. *J. Appl. Phys.* **2001**, *90*, 6466−6475.

(14) Spear, W. E.; Le Comber, P. G. *Solid State Commun.* **1975**, *17*, 1193−1196.

(15) Nadarajah, A.; Wu, M. Z. B.; Archila, K.; Kast, M. G.; Smith, A. M.; Chiang, T. H.; Keszler, D. A.; Wager, J. F.; Boettcher, S. W. *Chem. Mater.* **2015**, *27*, 5587−5596.

(16) Toroker, M. C.; Carter, E. a. *J. Mater. Chem. A* **2013**, *1*, 2474−2484.

(17) Wondraczek, L.; Mauro, J. C.; Eckert, J.; Kühn, U.; Horbach, J.; Deubener, J.; Rouxel, T. *Adv. Mater.* **2011**, *23*, 4578−4586.

(18) Rawson, H. *Inorganic Glass-Forming Systems*; Academic Press Inc.: London, 1967.

(19) Ropp, R. C. *Inorganic Polymeric Glasses*; Elsevier Science Publishers B.V.: Amsterdam, 1992.

(20) Doremus, R. H. *Glass Science*, 2nd ed.; John Wiley & Sons, Inc.: New York, 1994.

(21) Kim, N.; Bassiri, R.; Fejer, M. M.; Stebbins, J. F. *J. Non-Cryst. Solids* **2014**, *405*, 1−6.

(22) Murari, N. M.; Mansergh, R. H.; Huang, Y.; Kast, M. G.; Keszler, D. A.; Conley, J. F. *J. Mater. Res.* **2016**, 1−10.

DOI: 10.1021/jacs.6b11084
J. Am. Chem. Soc. 2016, 138, 16800−16808

(23) Smith, R. D. L.; Prévot, M.; Fagan, R. D.; Zhang, Z.; Sedach, P. A.; Siu, M. K. J.; Trudel, S.; Berlinguette, C. P. *Science* **2013**, *340*, 60−63.
(24) Jiang, K.; Zakutayev, A.; Stowers, J.; Anderson, M. D.; Tate, J.; McIntyre, D. H.; Johnson, D. C.; Keszler, D. A. *Solid State Sci.* **2009**, *11* (9), 1692−1699.
(25) Jiang, K.; Anderson, J. T.; Hoshino, K.; Li, D.; Wager, J. F.; Keszler, D. A. *Chem. Mater.* **2011**, *23* (4), 945−952.
(26) Schwartz, R. W.; Schneller, T.; Waser, R. *C. R. Chim.* **2004**, *7* (5), 433−461.
(27) Chueh, C.; Li, C.-Z.; Jen, A. K.-Y. *Energy Environ. Sci.* **2015**, *8*, 1160−1189.
(28) Battaglia, C.; de Nicolás, S. M.; De Wolf, S.; Yin, X.; Zheng, M.; Ballif, C.; Javey, A. *Appl. Phys. Lett.* **2014**, *104*, 1−5.
(29) Wurfel, U.; Cuevas, A.; Wurfel, P. *IEEE J. Photovoltaics* **2015**, *5* (1), 461−469.
(30) Sarou-Kanian, V.; Gleizes, A. N.; Florian, P.; Samélor, D.; Massiot, D.; Vahlas, C. *J. Phys. Chem. C* **2013**, *117*, 21965−21971.
(31) Zhou, N.; Kim, M.-G.; Loser, S.; Smith, J.; Yoshida, H.; Guo, X.; Song, C.; Jin, H.; Chen, Z.; Yoon, S. M.; Freeman, A. J.; Chang, R. P. H.; Facchetti, A.; Marks, T. J. *Proc. Natl. Acad. Sci. U. S. A.* **2015**, *112* (26), 7897−7902.
(32) Cargnello, M.; Fornasiero, P.; Gorte, R. J. *Catal. Lett.* **2012**, *142* (9), 1043−1048.
(33) Strayer, M. E.; Senftle, T. P.; Winterstein, J. P.; Vargas-Barbosa, N. M.; Sharma, R.; Rioux, R. M.; Janik, M. J.; Mallouk, T. E. *J. Am. Chem. Soc.* **2015**, *137*, 16216−16224.
(34) Greeley, J.; Stephens, I. E. L.; Bondarenko, a S.; Johansson, T. P.; Hansen, H. a; Jaramillo, T. F.; Rossmeisl, J.; Chorkendorff, I.; Nørskov, J. K. *Nat. Chem.* **2009**, *1*, 552−556.
(35) Ha, S. D.; Ramanathan, S. *J. Appl. Phys.* **2011**, *110*, 1−20.
(36) Strukov, D. B.; Snider, G. S.; Stewart, D. R.; Williams, R. S. *Nature* **2008**, *453* (May), 80−84.
(37) Richter, P.; Plassmeyer, P. N.; Harzdorf, J.; Rüffer, T.; Lang, H.; Kalbacova, J.; Jöhrmann, N.; Schulze, S.; Hietschold, M.; Arekapudi, S. S. P. K.; Albrecht, M.; Zahn, D. R. T.; Page, C. J.; Salvan, G. *Chem. Mater.* **2016**, *28* (14), 4917−4927.
(38) Prellier, W.; Fouchet, A.; Mercey, B. *J. Phys.: Condens. Matter* **2003**, *15*, R1583−R1601.
(39) Kobliska, R. J.; Aboaf, J. A.; Gangulee, A.; Cuomo, J. J.; Klokholm, E. *Appl. Phys. Lett.* **1978**, *33* (5), 473−475.
(40) Wang, W. Synthesis and Characterization of Aluminum Oxide Based Materials - from Molecule to Device. Ph.D. Thesis, Oregon State University, Corvallis, OR, 2013
(41) Wang, W.; Liu, W.; Chang, I.-Y.; Wills, L. A.; Zakharov, L. N.; Boettcher, S. W.; Cheong, P. H.-Y.; Fang, C.; Keszler, D. A. *Proc. Natl. Acad. Sci. U. S. A.* **2013**, *110* (46), 18397−18401.
(42) Wang, W.; Wentz, K. M.; Hayes, S. E.; Johnson, D. W.; Keszler, D. A. *Inorg. Chem.* **2011**, *50*, 4683−4685.
(43) Smith, S. W.; Wang, W.; Keszler, D. A.; Conley, J. F. *J. Vac. Sci. Technol., A* **2014**, *32* (4), 1−7.
(44) Schweitzer, G. K.; Lester, L. P. *The Aqueous Chemistry of the Elements*; Oxford University Press: New York, 2010.
(45) Carnes, M. E.; Knutson, C. C.; Nadarajah, A.; Jackson, M. N. J.; Oliveri, A. F.; Norelli, K. M.; Crockett, B. M.; Bauers, S. R.; Moreno-luna, H. A.; Taber, B. N.; Pacheco, D. J.; Olson, J. Z.; Brevick, K. R.; Sheehan, C. E.; Johnson, D. W.; Boettcher, S. W. *J. Mater. Chem. C* **2014**, *2*, 8492−8496.
(46) Plassmeyer, P. N.; Archila, K.; Wager, J. F.; Page, C. J. *ACS Appl. Mater. Interfaces* **2015**, *7*, 1678−1684.
(47) Nadarajah, A.; Carnes, M. E.; Kast, M. G.; Johnson, D. W.; Boettcher, S. W. *Chem. Mater.* **2013**, *25*, 4080−4087.
(48) Meyers, S. T.; Anderson, J. T.; Hong, D.; Hung, C. M.; Wager, J. F.; Keszler, D. A. *Chem. Mater.* **2007**, *19* (16), 4023−4029.
(49) Kojima, I.; Li, B. *The Rigaku Journal* **1999**, *16* (2), 31−42.
(50) van Hardeveld, R. M.; Gunter, P. L. J.; van IJzendoorn, L. J.; Wieldraaijer, W.; Kuipers, E. W.; Niemantsverdriet, J. W. *Appl. Surf. Sci.* **1995**, *84*, 339−346.
(51) Norelli, K. M.; Plassmeyer, P. N.; Woods, K. N.; Glassy, B. A.; Knutson, C. C.; Beekman, M.; Page, C. J. *Solid State Sci.* **2016**, *55*, 8−12.
(52) Melnikov, P.; Nascimento, V. A.; Arkhangelsky, I. V.; Consolo, L. Z. Z. *J. Therm. Anal. Calorim.* **2013**, *111*, 543−548.
(53) Yuvaraj, S.; Fan-Yuan, L.; Tsong-Huei, C.; Chuin-Tih, Y. *J. Phys. Chem. B* **2003**, *107*, 1044−1047.
(54) Will, G.; Masciocchi, N.; Parrish, W.; Hart, M. *J. Appl. Crystallogr.* **1987**, *20*, 394−401.
(55) Sasaki, S.; Fujino, K.; Takéuchi, Y. *Proc. Jpn. Acad., Ser. B* **1979**, *55* (2), 43−48.
(56) Åsbrink, S.; Norrby, L.-J. *Acta Crystallogr., Sect. B: Struct. Crystallogr. Cryst. Chem.* **1970**, *26*, 8−15.
(57) Bachmann, H. G.; Ahmed, F. R.; Barnes, W. H. *Zeitschrift für Krist. - Cryst. Mater.* **1961**, *115*, 110−131.
(58) Sawada, H. *Mater. Res. Bull.* **1994**, *29* (3), 239−245.
(59) Geller, S. *Acta Crystallogr., Sect. B: Struct. Crystallogr. Cryst. Chem.* **1971**, *27* (2), 821−828.
(60) Blake, R. L.; Hessevick, R. E.; Zoltai, T.; Finger, L. W. *Am. Mineral.* **1966**, *51*, 123−129.
(61) Abrahams, S. C.; Bernstein, J. L. *Acta Crystallogr., Sect. B: Struct. Crystallogr. Cryst. Chem.* **1969**, *25*, 1233−1236.
(62) Eaton, P.; West, P. *Atomic Force Microscopy*; Oxford University Press: Oxford, 2010.
(63) Zhang, L.; Jiang, H. C.; Liu, C.; Dong, J. W.; Chow, P. *J. Phys. D: Appl. Phys.* **2007**, *40*, 3707−3713.
(64) Alimardani, N.; Cowell, E. W., III; Wager, J. F.; Conley, J. F.; Evans, D. R.; Chin, M.; Kilpatrick, S. J.; Dubey, M. *J. Vac. Sci. Technol., A* **2012**, *30* (1), 1−6.
(65) Kim, J.-H.; Kim, J.-Y.; Kang, S.-W. *J. Appl. Phys.* **2005**, *97*, 1−5.
(66) Nilsen, O.; Rauwel, E.; Fjellvåg, H.; Kjekshus, A. *J. Mater. Chem.* **2007**, *17*, 1466−1475.
(67) Campbell, S. A. *The Science and Engineering of Microelectronic Fabrication*; Oxford University Press: New York, 2001.
(68) Haynes, W. M. *CRC Handbook of Chemisty and Physics*, 91st ed.; Taylor & Francis Group LLC: Boca Raton, 2016.
(69) Honda, K. *Bull. Chem. Soc. Jpn.* **1964**, *37* (5), 723−730.
(70) Zachariasen, W. H. *J. Am. Chem. Soc.* **1932**, *54* (1), 3841−3851.
(71) Stevels, J. M. *J. Phys. Colloid Chem.* **1949**, *53*, 591.
(72) Pauling, L. *J. Am. Chem. Soc.* **1929**, *51*, 1010−1026.
(73) Dunitz, J. D.; Orgel, L. E. *J. Phys. Chem. Solids* **1957**, *3*, 318−323.
(74) Paladino, A. E.; Kingery, W. D. *J. Chem. Phys.* **1962**, *37* (5), 957−962.
(75) Seevers, R.; DeNuzzio, J.; Farrington, G. C.; Dunn, B. *J. Solid State Chem.* **1983**, *N00014−81* (2), 1−19.
(76) Wuensch, B. J.; Vasilos, T. *J. Chem. Phys.* **1962**, *36* (11), 2917−2922.
(77) Rost, C. M.; Sachet, E.; Borman, T.; Moballegh, A.; Dickey, E. C.; Hou, D.; Jones, J. L.; Curtarolo, S.; Maria, J.-P. *Nat. Commun.* **2015**, *6*, 1−8.
(78) Bruce, P. G. *Solid State Electrochemistry*; University Press: Cambridge, 1995.

DOI: 10.1021/jacs.6b11084
J. Am. Chem. Soc. 2016, 138, 16800−16808